Sustainable Energy & Fuels

ROYAL SOCIETY OF CHEMISTRY

PAPER

View Article Online
View Journal | View Issue

Cite this: *Sustainable Energy Fuels*, 2026, **10**, 1453

Optimizing pyrolysis of sawdust and spent sulfite liquor: synergy, activation energy reduction and gas selectivity

Nampe Majoe, *[ab] Bilal Patel,[c] Joshua Gorimbo[c] and Isaac Beas [ad]

This study investigates the synergistic effects and pyrolysis kinetics of blends of sawdust (SD) and spent sulfite liquor (SSL) from a magnesium-based acid sulfite pulping process using thermogravimetric analysis (TGA). Experiments were conducted at heating rates of 5, 10, 15, 20, and 25 °C min^{-1} over a temperature range of 25–900 °C. The most favorable synergistic interaction was observed for the blend containing 80% SSL and 20% SD. Kinetic parameters were determined using model-free isoconversional methods (Friedman, Ozawa–Flynn–Wall, and Vyazovkin). The activation energies for SD were 180.10, 163.95, and 144.60 kJ mol^{-1}, while SSL exhibited higher values of 284.90, 241.33, and 222.28 kJ mol^{-1} for the respective models. Incorporating SD into SSL reduced the activation energy by approximately 20%, with the 80 : 20 blend showing values of 206.56, 195.66, and 177.31 kJ mol^{-1}. Char yield was unaffected by heating rate. Evolved gas analysis revealed distinct selectivity: the 80 : 20 blend favored hydrogen evolution (>0.06 wt%) near 550 °C which is 6 times more than SD alone, SD favored ethane (~0.18 wt%) at 400 °C, and SSL favored methane (~0.4 wt%) at 500 °C. These findings highlight the potential of SSL–SD blends for optimized pyrolysis performance and targeted gas production.

Received 16th November 2025
Accepted 24th January 2026

DOI: 10.1039/d5se01521a

rsc.li/sustainable-energy

1. Introduction

The advent of digitalization has led to a steady decline in writing paper production.[1] Nevertheless, the pulp and paper industry remains resilient by shifting its focus toward products such as packaging paper[2] and dissolving pulp.[3] Dissolving pulp, a key raw material used in industries likes textile and sanitary products,[4,5] requires cellulose with a purity level of approximately 98%, derived from wood.[6,7] Wood, which comprises roughly 50% cellulose, also contains hemicellulose and lignin that accounts for the remaining 50%.[8]

The two main commercial pulping processes used to obtain pure cellulose pulp is pre-hydrolysis Kraft (PHK) pulping and acid sulfite (AS) pulping.[9,10] The PHK process involves pre-hydrolyzing wood chips to remove the hemicellulose, followed by dissolving the lignin with a mixture of NaOH and Na_2S (white liquor) in a digester.[11] In contrast, the AS process employs different white liquor components, comprising of H_2SO_4 and Mg.[12] Both processes produce a by-product called spent liquor, a lignosulphonate compound bound to alkali metal sodium in PHK (called black liquor) and alkali earth metal magnesium in the AS process (called red, brown liquor or spent sulfite liquor). Currently, pulp and paper spent liquor is combusted in Tomlinson recovery boilers to generate energy and produce steam.[13] However, these recovery boilers face numerous drawbacks, including high maintenance costs, operational and safety challenges, and greenhouse gas emissions.[14]

Replacing the Tomlinson recovery boilers with advanced technologies to valorize spent liquor presents an opportunity to transform paper and pulp mills into biorefineries, capable of producing both energy, fuels and valuable green chemicals.[15] Various thermochemical conversion routes have been proposed for spent liquor, including gasification, supercritical water gasification, pyrolysis, hydrothermal liquefaction, hydrothermal carbonization, thermal hydrolysis, and wet oxidation.[16] Among these, pyrolysis stands out due to its ability to produce valuable products with lower emissions, offering notable environmental and energy benefits. Pyrolysis involves the thermal breakdown of organic matter in biomass, carried out in the absence of oxygen at temperature ranging between 300 °C and 800 °C,[17] yielding char, bio-oil, and gaseous products.[18] Its efficiency depends on factors such as temperature, heating rate, residence time, particle size, reactor type, pre-treatment, and catalysts.[19]

While pyrolysis of black liquor has been widely studied for biofuel and chemical production, research on SSL remains

[a]*Department of Chemical and Materials Engineering, University of South Africa (UNISA), Private Bag X6, Johannesburg, Florida 1710, South Africa. E-mail: nampem@dut.ac.za*

[b]*Green Engineering Research Group, Department of Chemical Engineering, Faculty of Engineering and the Built Environment, Durban University of Technology, Steve Biko Campus Block S4 Level 1, Box 1334, Durban, 4000, South Africa*

[c]*Institute for Catalysis and Energy Solutions (ICES), College of Science, Engineering and Technology, University of South Africa (UNISA), Private Bag X6, Johannesburg, Florida 1710, South Africa*

[d]*Department of Natural Resources & Materials, Botswana Institute for Technology Research and Innovation Gaborone, Botswana*

limited despite its industrial relevance. This gap underscores the need to explore SSL's pyrolytic potential. SSL contains magnesium, an alkali earth metal (AAEM) that may catalyse pyrolysis reactions. Previous studies have shown that AAEMs, including Ca and Mg, can lower decomposition temperatures and activation energies during biomass pyrolysis.[20,21] For example, Peng *et al.* (2014)[22] demonstrated sodium's catalytic effect in black liquor pyrolysis, enhancing phenol production at 350–450 °C. Similarly, Wang *et al.*[23] reported that $MgCl_2$ and $CaCl_2$ promote pyran ring-opening reactions, favouring furan formation and subsequent cleavage of C–C bonds.

Given the catalytic potential of magnesium and its ability to reduce activation energy,[24] investigating SSL pyrolysis kinetics is essential. Biomass pyrolysis involves complex reaction pathways and numerous intermediates,[25] making simple kinetic models inadequate.[26] Researchers have therefore adopted model-fitting and model-free approaches to determine kinetic triplets–activation energy (E_a), pre-exponential factor (A), and reaction mechanism ($f(\alpha)$).[27–29] Thermogravimetric analysis (TGA) is widely used to characterize pyrolysis behavior and determine the kinetic parameters.[30] Iso-conversional methods such as Friedman, Ozawa–Flynn–Wall (OFW), and Vyazovkin are commonly applied for biomass and black liquor studies.[30–33] However, the influence of inherent AAEMs in SSL during pyrolysis or co-pyrolysis with other biomasses remains unexplored.

In this work, SSL from magnesium-based acid sulfite pulping was blended with sawdust (SD), both being pulp and paper industry by-products. The study investigates the synergistic effect of SSL on pyrolysis behaviour using TGA and evaluates kinetic parameters *via* three model-free isoconversional methods (Friedman, OFW, and Vyazovkin). Additionally, evolved gas analysis was performed to identify gas selectivity during pyrolysis. The findings aim to provide theoretical insights and technical guidance for optimizing SSL–SD blends for sustainable energy and chemical production.

Table 1 The composition of sawdust and spent sulfite liquor blends

	The weight (%) of each component in mixed samples	
SSL blend (%)	Sawdust	Spent sulfite liquor (SSL)
0% SSL	100	0
50% SSL	50	50
60% SSL	40	60
70% SSL	30	70
80% SSL	20	80
90% SSL	10	90
100% SSL	0	100

2. Materials and methods

2.1. Material and sample preparation

Concentrated SSL (80% solids, 20% water) and sawdust (average particle size: 0.5–2 mm) were collected from a local pulp mill in KwaZulu Natal, South Africa. The SSL was manually mixed with sawdust (SD), in varying proportions. The different sawdust–SSL blends prepared are described in Table 1. The prepared mixture was transferred into a glass beaker and placed in an oven at 100 °C and dried overnight. After drying, the mixture was grinded using a ceramic pestle and mortar to achieve a homogeneous consistency and sieved to obtain particles smaller than 500 μm for characterization. The mixture was sealed in sample containers and stored in a controlled sample storeroom. Fig. 1 depicts different stages of the material during preparation.

2.2. Material characterization of ASP spent liquor and sawdust

The scanning electron microscopy (SEM) and energy dispersive X-ray spectroscopy (EDS) of the dried SSL was performed with the Zeiss Evo 10 SEM instrument to analyse the structure and determine the AAEM content in the spent sulfite liquor. The SEM was operated at an accelerating voltage of 15 kV, Amp time of 3.84 μs and resolution of 128.2 eV. The camera image was held at between 100–249× magnification. The elemental analysis (CHNS) of both dried SSL and sawdust was performed using a flash 2000 CHNS Elemental analyser (Thermo-Fisher Scientific). Each sample weighing between 1.75 g to 1.85 g were analysed separately. Proximity analysis was done by analysing the moisture content (M%), volatile matter (VM%) and fixed carbon (FC) based on the TGA data. The ash content was determined by taking the biomass into a furnace in presence of oxygen at 1000 °C for 7 hours to ensure all the volatile hydrocarbons are completely burned. The weight of remaining residue was the determined to obtain the ash content.

2.3. Thermogravimetric analysis

The change in mass of the various samples as temperature increases is monitored under an inert atmosphere using a TGA.

Fig. 1 Sawdust (1), mixed sawdust and sulfite spent liquor (2), dried mixture (3) and grinded mixture (4).

In this study, 15 mg of each sample was heated in a METTLER Toledo Thermogravimetric Analyzer (TGA/DSC3+) under inert atmosphere of nitrogen. The nitrogen gas was maintained at a temperature of 50 °C with a flowrate of 100 mL min^{-1}. The nitrogen gas eliminates entrapped gases in the system and prevents unwanted oxidation during the pyrolysis stage. Prior to conducting the experiments, the TGA/DSC3+ equipment was calibrated using an Indium reference standard.

Subsequently, the samples are heated from 25–900 °C using a range of heating rates (5, 10, 15, 20, 25 °C min^{-1}). Throughout the heating process, the TGA equipment continuously measured the sample mass and furnace temperature. Each experiment was run three times to ensure reproducibility. The TGA curves were plotted at different heating rates within the temperature range of 25–900 °C.

2.3.1. Synergy of co-pyrolysis process. The additive formula used to calculate the mixture profile in the absence of any synergistic effect is as follows:[34,35]

$$W_{cal} = x_1 W_1 + x_2 W_2 \quad (1)$$

The variations between the experimental weight (W_{exp}) and calculated weight (W_{cal}) for the blends at different heating rates is calculated by eqn (2), of which, the difference between W_{exp} and W_{calc} indicates a synergetic effect in the blend.

$$\Delta W = W_{exp} - x_1 W_1 + x_2 W_2 \quad (2)$$

where when; $\Delta W = 0$; the blend exhibits no synergistic interaction. $\Delta W > 0$; indicates a non-favourable synergistic effect. $\Delta W < 0$; signifies a favourable synergistic effect.

2.4. Kinetic analysis

The general rate equation, which combines the general mass law and Arrhenius eqn (3), is expressed as follows:[36,37]

$$\frac{d(\alpha)}{d(t)} = k(T) f(\alpha) = A \cdot f(\alpha) \cdot e^{\left(\frac{-E_a}{RT}\right)} \quad (3)$$

where; α is reaction fraction, t is time (s), $\frac{d(\alpha)}{d(t)}$ is rate of reaction, $k(T)$ is the rate constant (s^{-1}) and T is the reaction temperature (K), A is the pre-exponential factor (s^{-1}), $f(\alpha)$ is the kinetic model, which can take on various forms (see Table 1. in ref. 38), e is the logarithm base, E_a is the activation energy (kJ mol^{-1}), and R is the universal gas constant (kJ mol^{-1} K^{-1}).

Under non-isothermal conditions, where the sample is heated at a constant rate, eqn (3) can be transformed as follows:[39]

$$\frac{d(\alpha)}{dT} = \frac{A}{\beta} \cdot e^{\left(\frac{E_a}{RT}\right)} \cdot f(\alpha) \quad (4)$$

where; $\beta = \frac{dT}{dt}$ is the heating rate (°C s^{-1}).

2.4.1. Friedman method. Friedman method is an isoconversional approach based on the following general assumptions:

(1) The reaction conversion α at a certain heating rate β is a function of temperature;

(2) The conversion function $f(\alpha)$ and the kinetic parameters ($A$and E_a) are independent of the heating rate a fixed conversion [40]

For constant heating rate, and taking the natural logarithm on both sides of eqn (4) yields eqn (5):[41]

$$\ln\left(\beta \frac{d\alpha}{dT}\right) = \ln[A \cdot f(\alpha)] - \frac{E_a}{RT} \quad (5)$$

Thus, the eqn (5) can be re-written as eqn (6) to explicitly include the conversion factor α which is a Friedman equation:[42,43]

$$\ln\left[\left(\beta_i \frac{d\alpha}{dT}\right)_{\alpha,i}\right] = \ln[A_\alpha \cdot f(\alpha)] - \frac{E_a}{RT_{\alpha,i}} \quad (6)$$

Here, i represents the number assigned to each experiment, $T_{\alpha,i}$ is the temperature (K) at desired conversion α. Iso-conversional lines are obtained by plotting $\frac{d\alpha}{dt}$ *vs.* $1/T$ obtained from the TGA experimental data collected at different heating rates.[44] For each conversion α, the activation energy E_a is determined from the slope of $\ln\left[\left(\beta_i \frac{d\alpha}{dT}\right)_{\alpha,i}\right]$ *vs.* $-\frac{1}{RT_{\alpha,i}}$, where the intercept corresponds to $\ln[A_\alpha \cdot f(\alpha)]$. Data analysis for the Friedman method was conducted using THINKS software,[45,46] a free open source software.

2.4.2. Ozawa–Flynn–Wall (OFW) method. As mentioned earlier, OFW is an integral approach that assumes the activation energy is specific to a given degree of conversion. Assuming $f(\alpha)$ remains constant, eqn (2) can be rearranged as follows:[47,48]

$$g(\alpha) = \int_0^\alpha \frac{d\alpha}{f(\alpha)} = \int_{T_0}^{T} \frac{A}{\beta} \exp\left[-\frac{E_\alpha}{RT}\right] dT \quad (7)$$

Eqn (7) cannot be easily solved by analytical methods and requires numerical approximation techniques.[47] Several approximations has been developed, with the most widely used being the Ozawa–Flynn–Wall method, represented by eqn (8).[49,50]

$$\ln(\beta) = \ln\left(\frac{AE_\alpha}{g(\alpha)R}\right) - 5.331 - 1.052\frac{E_\alpha}{RT} \quad (8)$$

From eqn (8), the activation energy (E_α) can be determined from the slope of a linear fit of $\ln(\beta)$ *vs.* $1/T$

2.4.3. Vyazovkin method. This advanced isoconversional integral method is a widely recommended for the accurate determination of activation energies (E_α). It assumes that the reaction model $g(\alpha)$ is independent of a heating rate β.[51] Based on this assumption $g(\alpha)$ remains constant at a specific conversion. By replacing the temperature integral in eqn (8) with Doyle's approximation,[52] eqn (9) can be rewritten as:

$$I(E,T) \approx \left(\frac{E}{R}\right)\exp\left(-5.331 - \frac{1.052E}{RT}\right) \quad (9)$$

Table 2 Representation of key evolved gases and their ion fragments

m/*z*	Ion fragments	Representative species
64	SO_2^+	Sulfur dioxide
44	CO_2^+	Carbon dioxide
27	$C_2H_6^+$	Ethane
18	H_2O^+	Water
15	CH_4^+	Methane
2	H_2^+	Hydrogen

From eqn (9), along with a series of assumptions and derivations, Vyazovkin (1997) formulated the following expression eqn (10):[52]

$$\Omega = \sum_{i=1}^{n} \sum_{j \neq i}^{n} \frac{I(E_\alpha, T_{\alpha,i})\beta_j}{I(E_\alpha, T_{\alpha,j})\beta_i} = \min \quad (10)$$

In eqn (10), i and j represent independent experimental runs performed at different heating rates, β. Data analysis for OFW and Vyazovkin was performed using Kinetic Calculation software,[53] a free open source thermo-kinetic software.

2.5. Evolved gases analysis

The evolved gases during thermal decomposition were analyzed using a thermogravimetric analyzer (TGA) coupled with a mass spectrometer (MS). Approximately 15 mg of each sample–sawdust (SD), 100% spent sulfite liquor (SSL), and a blend of SSL and SD at 80 : 20 ratio (SSL: SD)-was placed in the TGA-MS system. The samples were heated from ambient temperature to the target temperature at a constant heating rate of 50 °C min^{-1} under an inert atmosphere of nitrogen flowing at 15 mL min^{-1}. The MS continuously monitored the gases evolved during thermal degradation, enabling identification of major species released at different temperature ranges. Table 2 shows the ions set to be scanned and their corresponding evolved gas species in the bases of their mass to charge ratio (*m*/*z*).

Nature of quadrupole mass spectrometry (QMS) data and normalization: evolved gas composition was monitored by quadrupole MS (Faraday detector, EI 70 eV) at *m*/*z* 64 (SO_2), 44 (CO_2), 27 ($C_2H_3^+$ from C_2H_6), 29 (CO^+), 18 (H_2O^+), 15 (CH_3^+ from CH_4), and 2 (H_2^+). Signals reported as "Corrected Data", "%" reflect the instrument's internal normalization; the calibration type was set to "Single-Point" (factor = 1) for all channels in this dataset, and no external sensitivity or fragmentation calibration was applied. Consequently, these results are semi-quantitative and are used to compare relative trends and onset/peak positions only. We do not interpret the wt% as absolute wt% but as corrected data % values, since there was no calibration. Where absolute yields are required, per-species calibration with known gas mixtures and fragmentation corrections are needed to convert ion current to mass and normalize to sample mass. CO was not included in the results since it presented large data due to CO and N_2 sharing the same peak at *m*/*z* of 29.

3. Results and discussions

3.1. Material characterization

SEM images at different magnifications (100–245×) are presented in Fig. 2, illustrating the surface morphology and

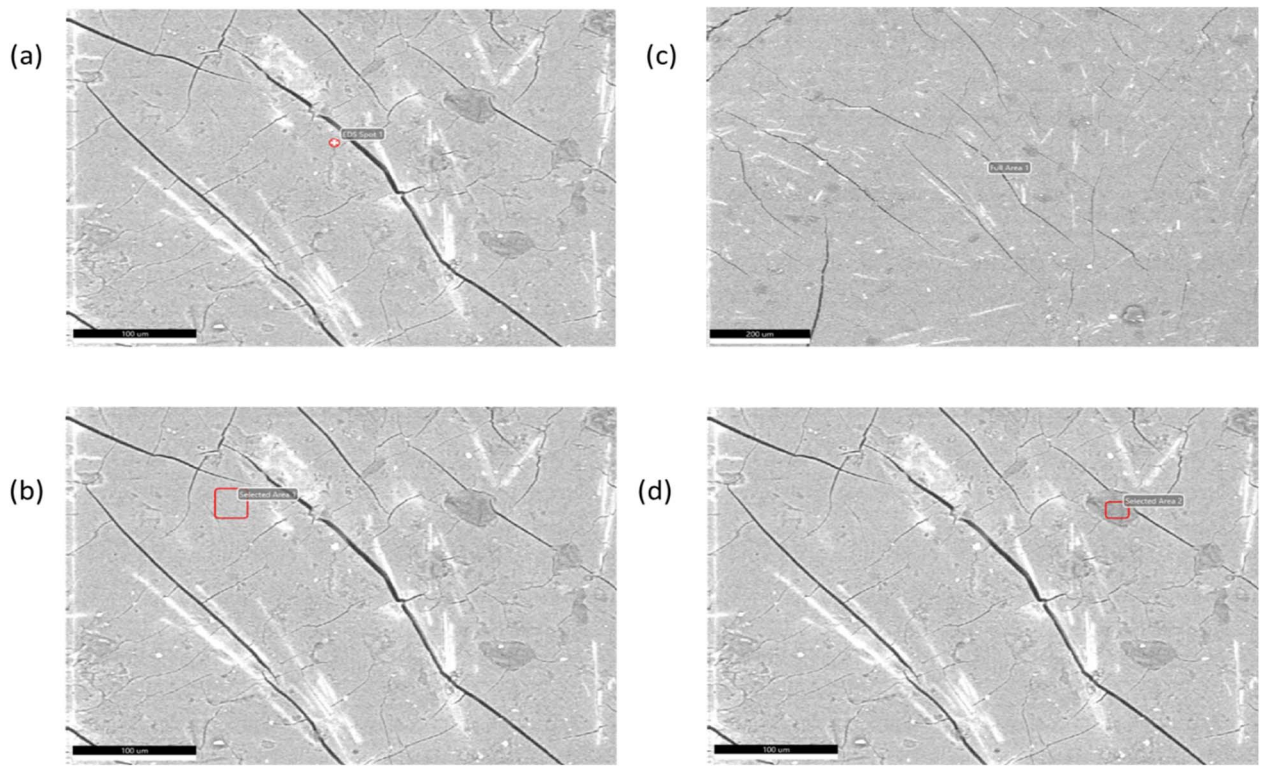

Fig. 2 Dried SSL SEM images at different positions and resolution (a) (EDS) spot 1 at 100 μm, (b) selected area 1 at 100 μm, (c) full area 1 at 200 μm and (d) selected area 2 'darker spot' at 100 μm.

Table 3 Representation of SSL elemental analysis at different positions and resolution (a) EDS spot 1 at 100 μm, (b) selected area 1 at 100 μm, (c) full area 1 at 200 μm and (d) selected area 2 'darker spot' at 100 μm

Element	Image symbol	Weight%	Atom%	Error%
C	(a)	35.81	74.45	9.82
	(b)	36.99	48.02	9.81
	(c)	36.79	46.27	8.74
	(d)	70.78	78.26	6.66
Average		**45.09**	**61.75**	**8.76**
O	(a)	38.54	38.33	9.03
	(b)	42.20	41.13	9.19
	(c)	49.03	46.29	8.62
	(d)	22.73	18.87	11.59
Average		**38.13**	**36.16**	**9.61**
Mg	(a)	6.65	4.35	5.10
	(b)	5.12	3.28	5.84
	(c)	4.81	2.99	5.65
	(d)	1.42	0.78	6.64
Average		**4.5**	**2.85**	**5.81**
Al	(a)	0.47	0.28	11.18
	(b)	—	—	—
	(c)	0.47	0.26	10.33
	(d)	0.49	0.24	7.85
Average		**0.36**	**0.17**	**6.06**
Si	(a)	6.33	3.59	3.68
	(b)	—	—	—
	(c)	0.49	0.26	7.6
	(d)	—	—	—
Average		**1.705**	**0.96**	**2.82**
S	(a)	11.58	5.75	2.77
	(b)	14.89	7.24	2.51
	(c)	8.01	3.78	2.61
	(d)	3.79	1.57	3.25
Average		**9.57**	**4.59**	**2.79**
K	(a)	0.62	0.25	10.58
	(b)	0.8	0.32	15.64
	(c)	0.39	0.15	12.64
	(d)	0.39	0.13	14.57
Average		**0.55**	**0.21**	**13.35**
Cl	(a)	—	—	—
	(b)	—	—	—
	(c)	0.40	0.15	23.86
	(d)	—	—	—
Average		**0.10**	**0.04**	**5.97**

elemental distribution of the SSL. Energy-dispersive X-ray spectroscopy (EDS) was employed to identify the elements present in the sample and quantify their concentrations.

Fig. 2(a) shows the elemental composition at a specific spot, where aluminum and silicon were detected at 0.47 wt% and 6.33 wt% respectively. However, when the imaging field was shifted to selected area 1 (Fig. 2(b)), these elements were absent, as confirmed in Table 3. Increasing the focus length to 200 μm (Fig. 2(c)) revealed aluminum at the same concentration (0.47 wt%) but a significantly reduced silicon concentration of 0.49 wt%. Imaging at a darker region (Fig. 2(d)) indicated a notably higher carbon concentration—almost double that observed in other areas.

Fig. 2(a–c) show that magnesium concentrations range between 4.81–6.65 wt%, whereas at the darker spot, the concentration decreases to 1.42 wt%.

Table 4 Ultimate and proximate analysis of sawdust and SSL

Characteristics	Sawdust (wt%)	SSL (wt%)
Proximate composition (%)		
Moisture	7	10
Volatile matter	76.3	48
Fixed carbon	16.7	39
Ash	0	3
Elemental composition (%)		
Carbon	43.5	31.6
Hydrogen	5.2	6.2
Nitrogen	0.2	0.2
Oxygen (by difference)	51.1	52.5
Sulfur	0	5.0

The results of the ultimate analysis of sawdust and SSL are presented in Table 4. Typically, the oxygen-to-carbon (O/C) and hydrogen-to-carbon (H/C) ratios are used to evaluate the energy content of a fuel, with a higher O/C ratio indicating lower energy potential. The analysis revealed that SSL contained 5% sulfur, 0.2% nitrogen, and 53% oxygen, which aligns with findings reported by.[54] The carbon content of SSL was slightly lower at 31.6%; however, EDS analysis indicated a higher average carbon content of 45.09% (see Table 3).

Table 3 summarizes the elemental composition of SSL obtained from SEM-EDS imaging and bulk elemental analysis. Differences between the two techniques, particularly for carbon (C) and oxygen (O), are expected due to the inherent characteristics of each method. SEM-EDS provides a localized surface elemental profile rather than the overall sample composition. In this study, measurements were taken at four distinct points on the sample surface and averaged to improve representativeness. Conversely, elemental analysis determines the bulk composition, yielding values of 31.6% for C and 52.5% for O, which differ from SEM-EDS results. These variations highlight the complementary nature of the two techniques: SEM-EDS is valuable for surface characterization, while elemental analysis offers a more accurate representation of the overall material.

The hydrogen content was 6.2%, which is higher than values reported by Duangkaew *et al.* (2023).[54] For proximate analysis, AS spent liquor exhibited higher fixed carbon compared to sawdust, whereas volatile matter was greater in sawdust (76.3%) than in AS spent liquor (48%). Similar proximate analysis results for sawdust were reported by Varma *et al.* (2019).[55] Le Roux *et al.* (2024) reported higher moisture,[56] volatile, and ash contents for SSL, with moisture at 43.3%, volatiles at 61.0%, and ash at 6.5%. Differences in proximate analysis may be attributed to sampling point variations, as higher moisture suggests SSL was sampled prior to the evaporators following the pulping process.

The composition of sawdust in this study is consistent with previously published data.[55,57]

3.2. Thermogravimetric analysis

Fig. 3(a) shows the mass loss curves for sawdust (SD), SSL, and their blends at a heating rate of 5 °C min^{-1}. SSL exhibited the

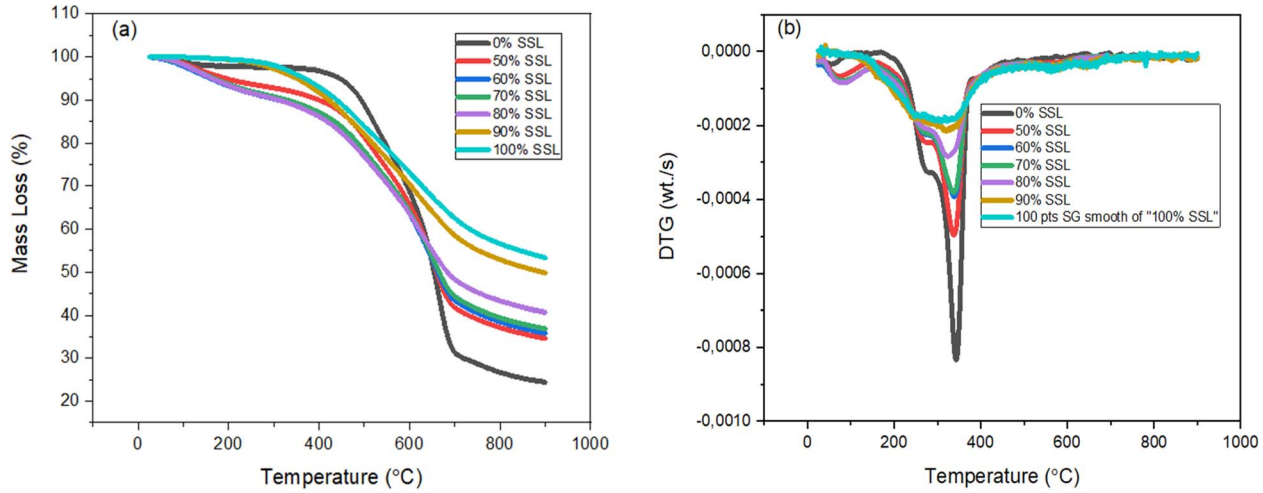

Fig. 3 TGA analysis: (a) mass loss curves for pyrolysis of SSL and sawdust, as well as their blends at heating rate of 5 °C min^{-1}, (b) DTG curves for individual SSL and sawdust at heating rate of 5 °C min^{-1}.

Table 5 Degradation parameters at different stages of sawdust, sulfite spent liquor, and their blends at heating rate of 5 °C min^{-1}

Stage	Parameters	0% BL	50% BL	60% BL	70% BL	80% BL	90% BL	100% BL
First (I)	T_{range} (°C)	37–107	38–150	38–159	37–154	38–153	—	—
	W_{Loss} (%)	1.91	6.55	9.10	8.48	8.90	—	—
	DR_{max} (s^{-1})	-3.42×10^{-5}	-6.61×10^{-5}	-8.05×10^{-5}	-7.82×10^{-5}	-8.34×10^{-5}	—	—
	T_{max}	57	76	79	80	80	—	—
Second (II)	T_{range} (°C)	178–451	162–439	161–455	159–480	156–462	113–520	145–458
	W_{Loss} (%)	72.73	57.22	54.21	54.88	50.01	52.46	45.21
	DR_{max} (s^{-1})	-8.34×10^{-4}	-4.93×10^{-4}	-3.89×10^{-4}	-3.81×10^{-4}	-2.83×10^{-4}	-2.11×10^{-4}	-1.91×10^{-4}
	T_{max} (°C)	344	340	341	339	325	323	302
Third (III)	T_{range} (°C)	452–900	508–900	460–900	500–900	518–900	525–900	505–900
	W_{Loss} (%)	8.71	8.59	11.06	9.13	9.80	11.20	11.94
	DR_{max} (s^{-1})	—	—	—	—	—	—	—
	T_{max} (°C)	—	—	—	—	—	—	—
% Residual weight at 900 °C		16.07	24.27	24.89	26.26	28.55	35.49	39.18

highest char yield (39%), while sawdust had the lowest (16%). SSL, a byproduct of the pulping process, has a complex composition comprising 38–47% lignin, 30–35% aliphatic carboxylic acids, and 5–10% hemicellulose-derived residues and extractives.[58] The low content of cellulose in SSL makes it more resistant to thermal decomposition, explaining its higher char yield. Sawdust, with its higher cellulose content, decomposed more rapidly than SSL, which contains more lignin. SSL exhibited slower weight loss over a broader temperature range.

Yang *et al.* (2007)[59] reported that hemicellulose decomposes first (220–315 °C), cellulose decomposes rapidly at higher temperatures (315–400 °C), and lignin decomposes slowly across a wide range due to its methoxyl (–O–CH_3), C–O–C, and C=O groups in aromatic rings.[59] This trend is reflected in Fig. 3(a).

Fig. 3(b) presents the derivative thermogravimetric (DTG) curves, revealing three distinct stages:

• Stage I (120–130 °C): drying phase.[60]

• Stage II (200–500 °C): active pyrolysis zone, where most hemicellulose, cellulose, and part of lignin decompose.[35,61] This is driven by cleavage of weak ether bonds (R–O–R, 380–420 kJ mol^{-1}) in lignocellulosic biomass. Hemicellulose decomposes first due to weaker bonds, followed by cellulose and lignin 61.

• Stage III (>500 °C): slow degradation of lignin, attributed to its aromatic structure and phenolic hydroxyl groups.[61–63]

DTG curves for blends show decreasing peak intensity with increasing SSL content. SSL (lignosulphonate) contains lignin, aliphatic carboxylic acids, and some polysaccharides. Alén *et al.* (1995) noted that alkali metals in black liquor shift decomposition of aliphatic acids from 150–300 °C to 250–550 °C.[64] Thus, higher SSL content increases lignin and aliphatic components, delaying decomposition beyond 500 °C and reducing DTG peak intensity. Yang *et al.* (2007) further observed that lignin decomposes over a broad range (100–900 °C), while cellulose and hemicellulose decompose more easily, releasing CO, CO_2, and hydrocarbons.[59] Above 500 °C, H_2 is released, and above 600 °C, CO evolves[59] (see gas evolution later). These gases may interact with SSL compounds, aiding aromatic ring breakdown and reducing char formation.

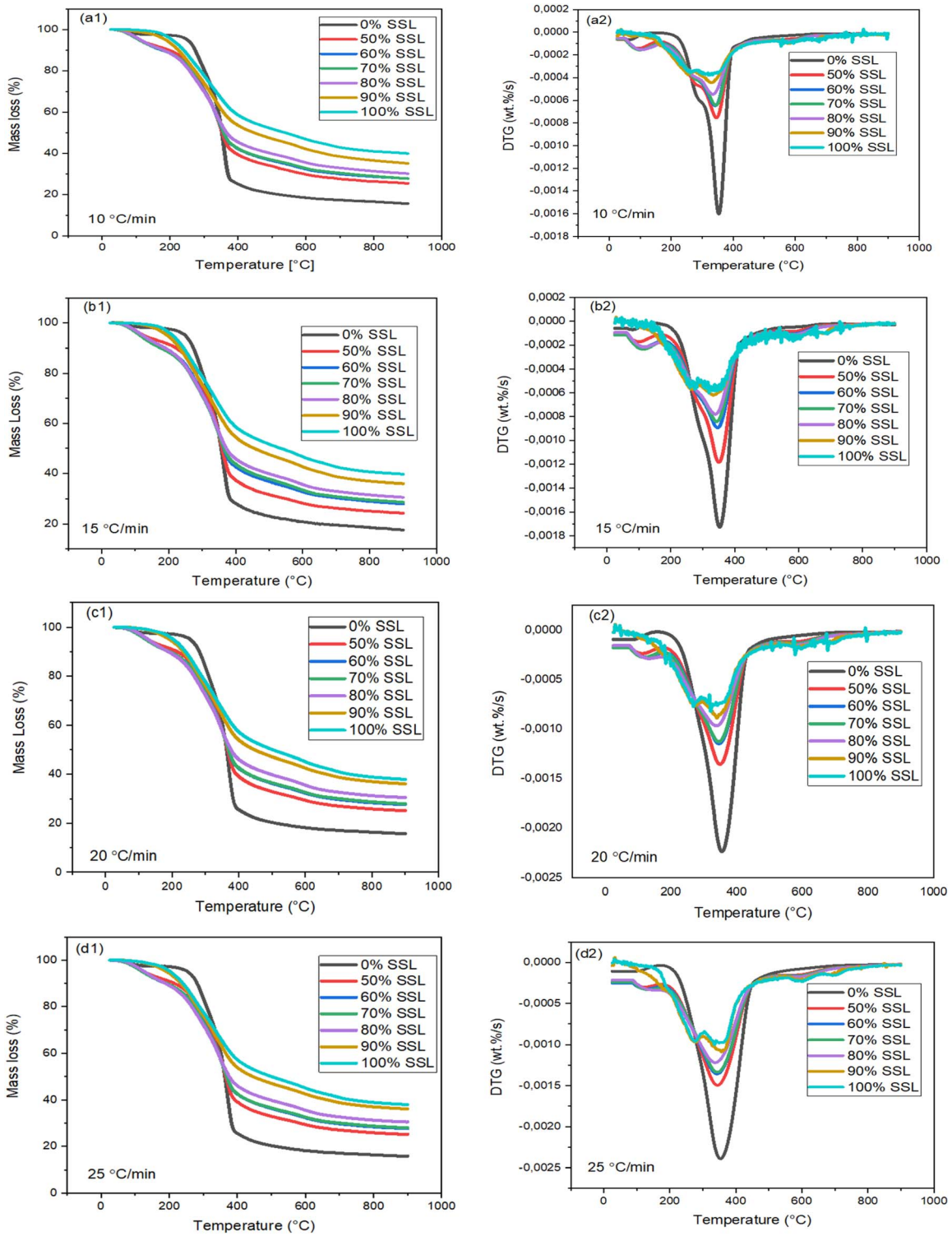

Fig. 4 TG analysis of SSL and sawdust at four different heating rates (a) 10, (b) 15, (c) 20, (d) 25 °C min^{-1}: mass loss as a function of temperature (a1, b1, c1 and d1) and DTG (a2, b2, c2 and d2).

The sawdust DTG curve shows a shoulder near 250 °C, likely due to hemicellulose, and a sharp peak from rapid cellulose degradation.[61]

Table 5 summarizes T_{max} and DR_{max} for SD, SSL, and blends across three stages (drying, active devolatilization, char decomposition). Weight loss in stage I increases with SSL addition, likely due to higher moisture content, which also raises T_{max}. Stage II weight loss decreases as SSL increases, reflecting higher lignin content that decomposes later. T_{max} in stage II decreases with SSL addition, suggesting a synergistic effect. Char yield at 900 °C follows the trend SD < blends < SSL, confirming that higher lignin content contributes to greater char formation.

Table 6 Residual weight % at 900 °C and T_{max} (°C) in second pyrolysis stage at different heating rates

Heating rate (°C)		0% BL	50% BL	60% BL	70% BL	80% BL	90% BL	100% BL
5	Weight %	16.07	24.27	24.89	26.26	28.55	35.49	39.18
	T_{max} (°C)	344	340	341	339	325	323	303
10	Weight %	15.48	25.34	27.70	27.64	30.05	35.05	39.82
	T_{max} (°C)	354	345	341	343	334	329	321
15	Weight %	17.53	24.22	27.99	28.66	30.57	35.99	39.74
	T_{max} (°C)	335	350	347	345	340	333	321
20	Weight %	15.88	25.23	27.78	28.05	30.57	36.11	37.93
	T_{max} (°C)	358	358	349	349	340	341	321
25	Weight %	17.70	25.90	27.60	28.31	30.10	36.10	39.62
	T_{max} (°C)	356	345	345	345	338	357	334

3.2.1. Effect of heating rates on co-pyrolysis. Fig. 4 shows the TGA profiles for SSL, sawdust, and their blends at different heating rates. The DTG peaks (T_{max}) shift to higher devolatilization temperatures as the heating rate increases from 5 to 25 °C min^{-1}, as summarized in Table 5 and Fig. 4(a–d) also illustrate peak broadening, indicating that at higher heating rates, the consumption rates of hemicellulose and cellulose become more similar. This behaviour is characteristic of non-isothermal conditions, as reported by other researchers.[34,35]

The shift in DTG curves is primarily attributed to the poor thermal conductivity of biomass, which affects heat transfer across the cross-section of SSL and sawdust. At lower heating rates, the temperature profile within SSL, sawdust, and their blends can be assumed to be nearly linear due to the slower heating, allowing more uniform heat distribution throughout the sample.[61] Conversely, at higher heating rates, insufficient time for heat transfer results in a non-linear temperature profile, with the inner core remaining cooler than the outer layers.[61]

Table 6 also shows that the residual weight percentage at 900 °C increases with heating rate (5–25 °C min^{-1}).

3.2.2. Synergy of co-pyrolysis process. Fig. 5 illustrates the distinct thermal behaviours of sawdust and SSL, which arise from differences in their composition, structure, and physicochemical properties. To evaluate the synergistic effect in the blends, an additive model eqn (1) was applied, assuming no interaction between sawdust and SSL. The experimental thermal profiles were then compared with those predicted by the additive model. Deviations between these profiles indicate the presence of synergistic interactions.

The parameter ΔW represents the interaction effect during thermal degradation. When $\Delta W = 0$, the blend exhibits no synergy, behaving as a simple additive mixture. A $\Delta W > 0$ indicates an unfavourable synergistic effect, where degradation is less efficient than expected. Conversely, a $\Delta W < 0$ signifies a favourable synergistic effect, implying enhanced degradation due to improved interaction between sawdust and SSL.

Fig. 5(a1–e1) shows the synergistic effect for different blends at 5 °C min^{-1}. The strongest synergy occurs between 100 °C and 400 °C, corresponding to the decomposition of hemicellulose and cellulose. Increasing SSL concentration reduces the synergistic effect, likely due to higher lignin content, which is more resistant to thermal degradation—particularly evident between 400 °C and 900 °C. Fig. 6 illustrates the synergistic effects across various heating rates. Favourable synergy is observed in all blends except the 90% SSL blend, which shows minimal interaction at lower temperatures and becomes favourable only around 200 °C (at 5, 15, and 20 °C min^{-1}) and above 550 °C at 20 °C min^{-1}. The effect is most pronounced during the initial decomposition stage (up to ~380 °C), when hemicellulose (220–315 °C) and cellulose (315–400 °C) degrade.[59] These trends align with the DTG profiles discussed in Fig. 3 and 4.

Song *et al.* (2014)[62] reported that co-pyrolysis of pine sawdust with lignite promotes the release of H and OH radicals, which act as hydrogen donors and facilitate cracking of aromatic rings in coal. These radicals interact with lignite, reducing its carbon content due to higher H/C and O/C ratios and the presence of alkali and alkaline earth metals (AAEMs) in sawdust.[63] Similarly, blends with lower sawdust content exhibit weaker synergy, while blends containing 70–80% SSL show the highest synergistic effect in terms of residual weight. This may be attributed to an optimal sawdust-to-SSL ratio and the presence of magnesium in SSL.

Fig. 5 also shows that blends with 90% SSL have ΔW values close to zero, particularly at the beginning and end of pyrolysis, suggesting that SSL primarily decomposes independently due to the limited sawdust content.

3.3. Kinetic analysis

The activation energy (E_a) was determined at various conversion levels as outlined in Sections 2.3–2.4. Fig. 7 presents the linear plots generated using the Friedman method over the conversion range $\alpha = 0.05$–0.65, along with conversion–temperature plots and apparent activation energies obtained from different isoconversional methods for both sawdust and SSL. As described in Section 2.3, eqn (6) allows for the computation of $\frac{d\alpha}{dt}$ *vs.* $1/T$ from TGA data, using THINKS software.

For $\alpha = 0.65$, the software did not yield values, likely due to low correlation coefficients. This observation is consistent with the findings of Khiari and Jeguirim (2018),[65] who conducted a kinetic analysis of grape marc from the Tunisian wine industry–a material rich in lignocellulosic compounds. They concluded that data beyond $\alpha = 0.65$ lacked reliable determination coefficients due to the complex nature of char production and rearrangement.[65] Error bars are not shown in the Friedman plots because the data are derived from numerically

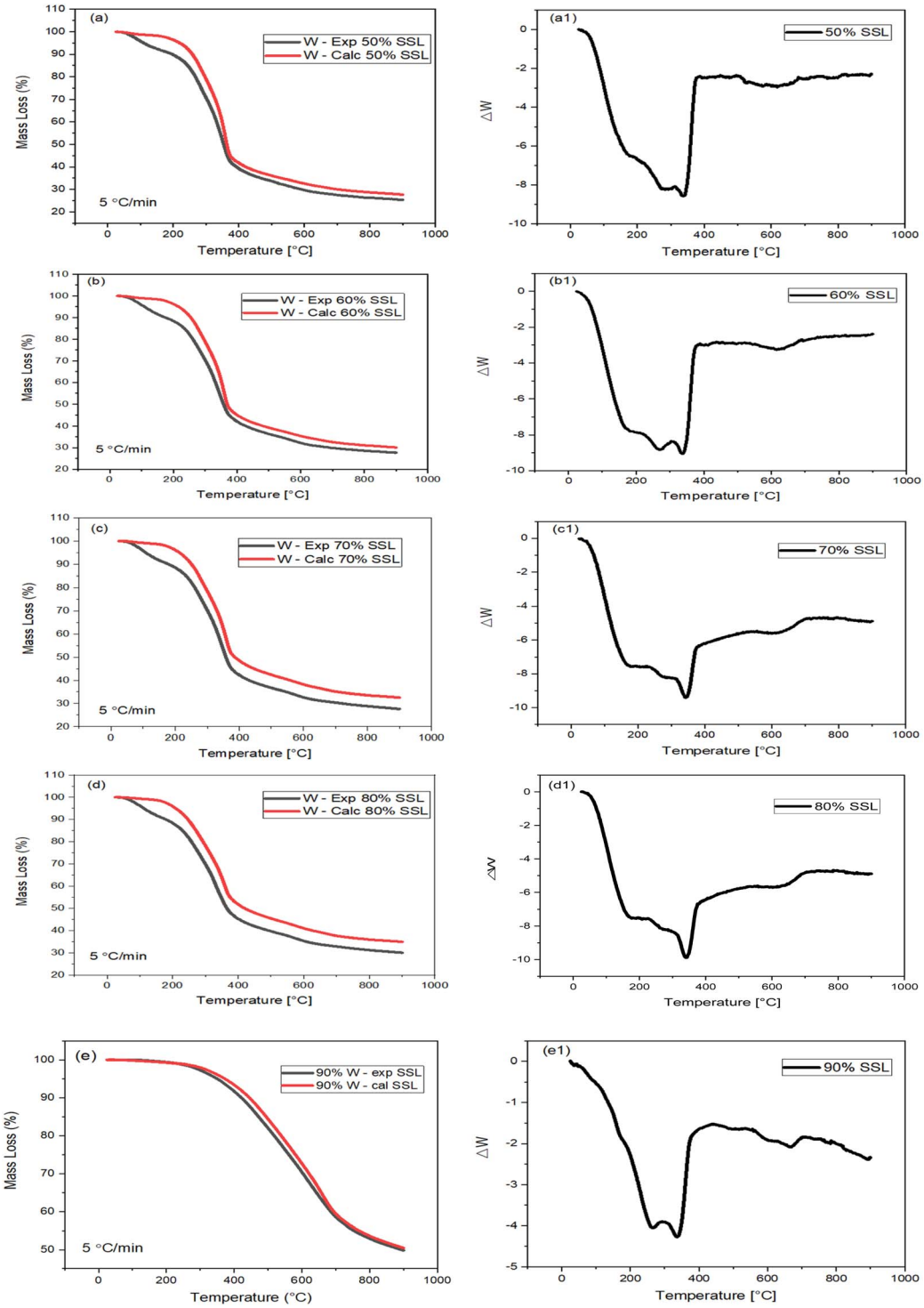

Fig. 5 Experimental and calculated weight % TGA and synergetic effect curves for five different blends of sawdust and SSL (a and a1) 50% SSL, (b and b1) 60% SSL, (c and c1) 70% SSL, (d and d1) 80% SSL, (e and e1) 90% SSL at 5 °C min^{-1} heating rate.

differentiated rate curves and regression analysis across multiple heating rates; therefore, uncertainty is associated with the calculated activation energy values from the slope rather than with individual plotted points.

3.3.1. Blends friedman linear plots for calculating E_a. Fig. 8, presents Friedman linear plots for blends of sawdust and SSL. The plots indicate relatively constant conversions between $\alpha = 0.2$–0.5, which is likely due to the homogeneous degradation of hemicellulose and cellulose in both components. At $\alpha = 0.05$, the consistent degradation observed across all blends (regardless of SSL proportion) can be attributed to moisture removal. Beyond $\alpha = 0.5$, lignin degradation becomes increasingly difficult. This resistance is associated with the high carbon content of char, which enhances thermal stability compared to

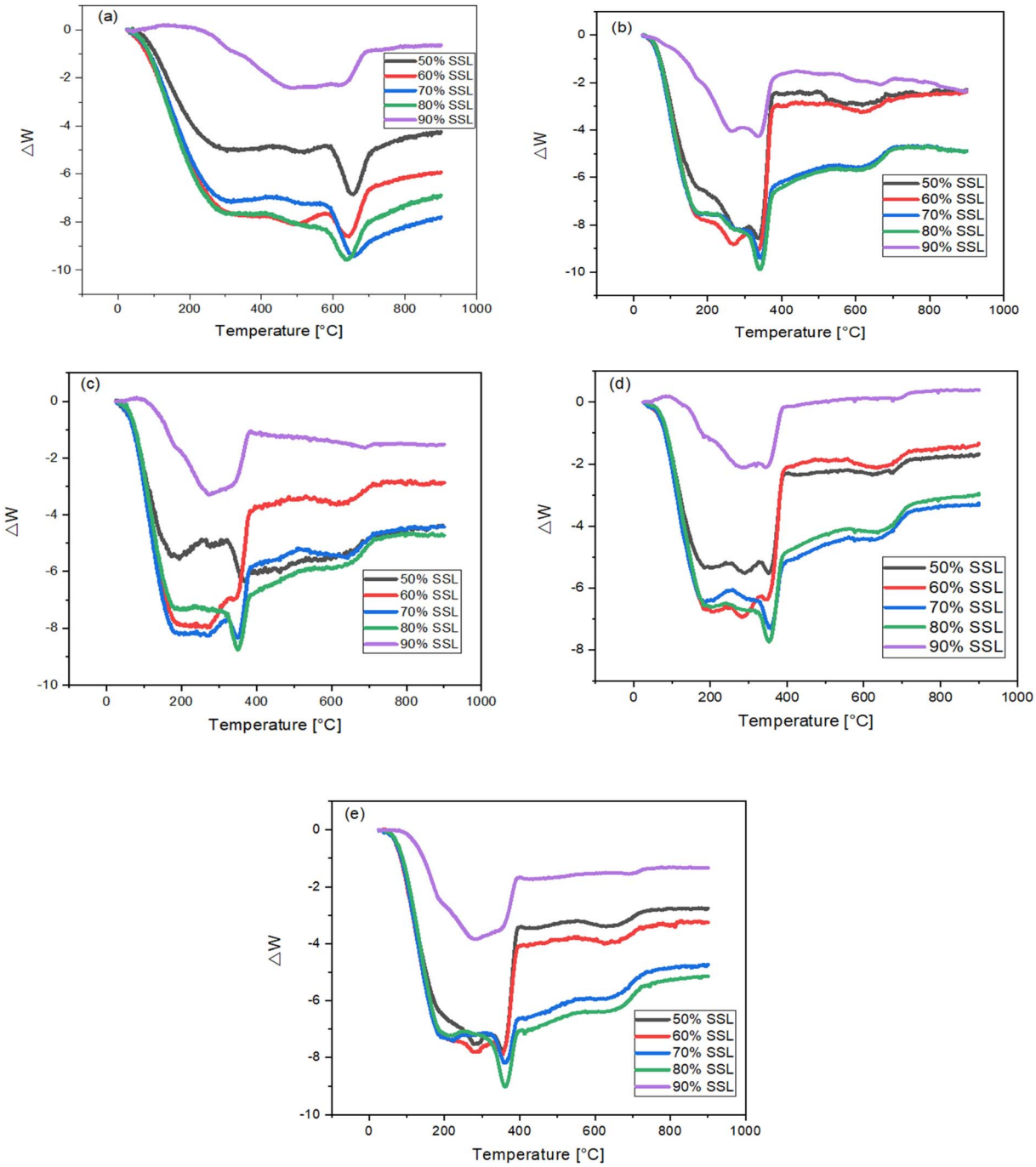

Fig. 6 Synergetic effect of sawdust and SSL in the blends at different heating rates of (a) 5, (b) 10, (c) 15, (d) 20, (e) 25 °C min^{-1}.

sawdust and SSL. Furthermore, at higher conversion levels, the presence of aromatic rings in lignin molecules may hinder further decomposition.

The conversion profiles in Fig. 8 for sawdust and SSL show that conversions corresponding to Friedman plots (α = 0.2–0.65) occur within a temperature range of 210–400 °C. This range corresponds to the second stage of thermal decomposition for both materials, during which hemicellulose, cellulose, and lignin begin to degrade.

3.3.2. Activation energy determination using friedman method. Fig. 9 illustrates the variation in apparent activation energy for sawdust and SSL, calculated using the Friedman isoconversional method *via* THINKS software. For sawdust, activation energy ranged from 171.42 to 185.75 kJ mol^{-1}, with an average of 180.09 kJ mol^{-1}. Nyombi *et al.* (2018)[66] reported a mean activation energy of 198 kJ mol^{-1} for Ash (Fraxinus) wood sawdust under similar TGA heating rates, while Wang *et al.* (2022)[67] found values between 180–282 kJ mol^{-1} for pinewood sawdust using the same Friedman approach.

For SSL, activation energy ranged from 209.84 to 462.59 kJ mol^{-1}, averaging 284.90 kJ mol^{-1}. Although no direct literature values for SSL were found, Yang *et al.* (2021)[68] investigated

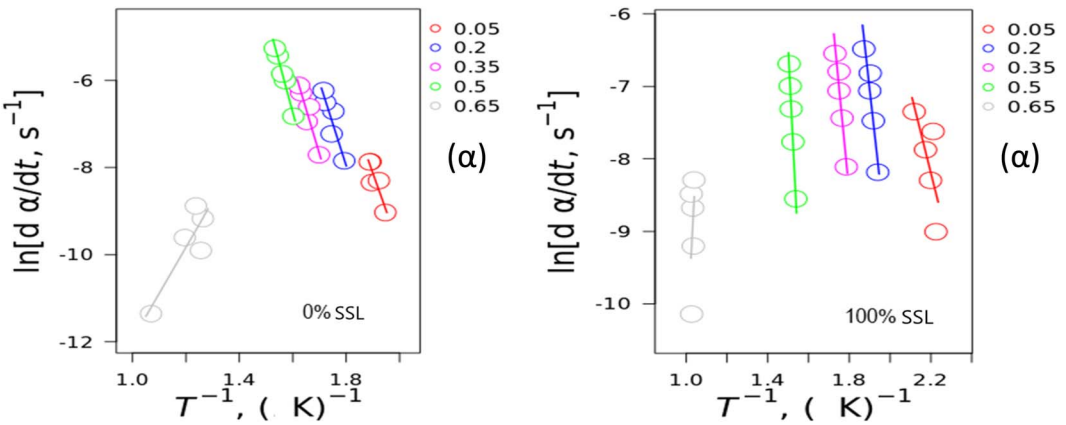

Fig. 7 Linear plots for calculating E_a for 0% SSL and 100% SSL using Friedman method.

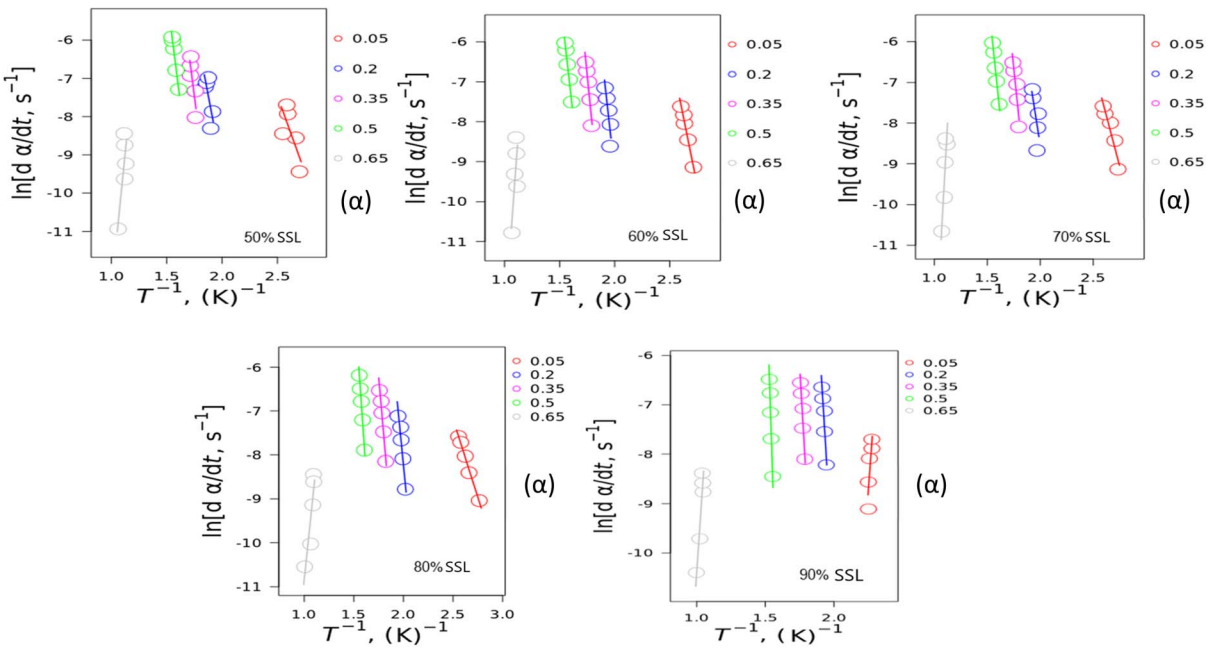

Fig. 8 Different blends ratio of SSL and sawdust for calculating E_a, using Friedman method 50% SSL, 60% SSL, 70% SSL, 80% SSL, 90% SSL.

lignin isolated from cellulose composite films and reported activation energies between 182.15–240.63 kJ mol^{-1} for $\alpha = 0.2$–0.65, which aligns closely with the lower range observed in this study. The consistently high activation energy for 100% SSL across all conversions likely reflects its high lignin content. This observation is supported by TG/DTG profiles, which show SSL exhibiting slower degradation and higher peak temperatures compared to sawdust.

3.3.3. Activation energy determination using OFW and Vyazovkin method. The activation energies calculated using the OFW and Vyazovkin methods were obtained through an open-access kinetic analysis tool.[53] Fig. 10 compares the E_a values for sawdust derived from both methods. The mean activation energy determined by the OFW method was 163.95 kJ mol^{-1} for sawdust and 241.33 kJ mol^{-1} for SSL. In comparison, the Vyazovkin method yielded slightly lower mean values: 144.60 kJ mol^{-1} for sawdust and 222.28 kJ mol^{-1} for SSL.

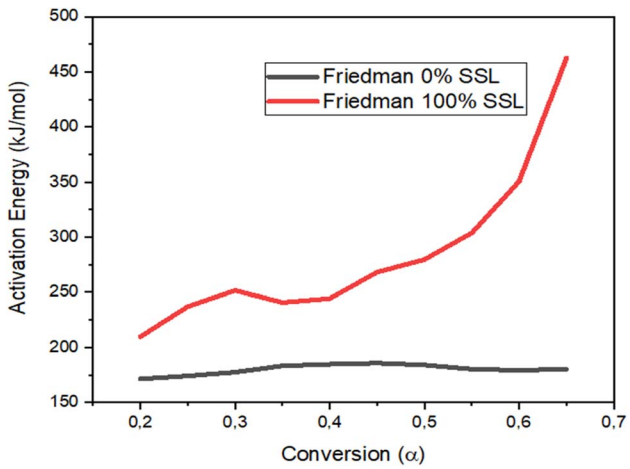

Fig. 9 Friedman activation energies for sawdust and SSL.

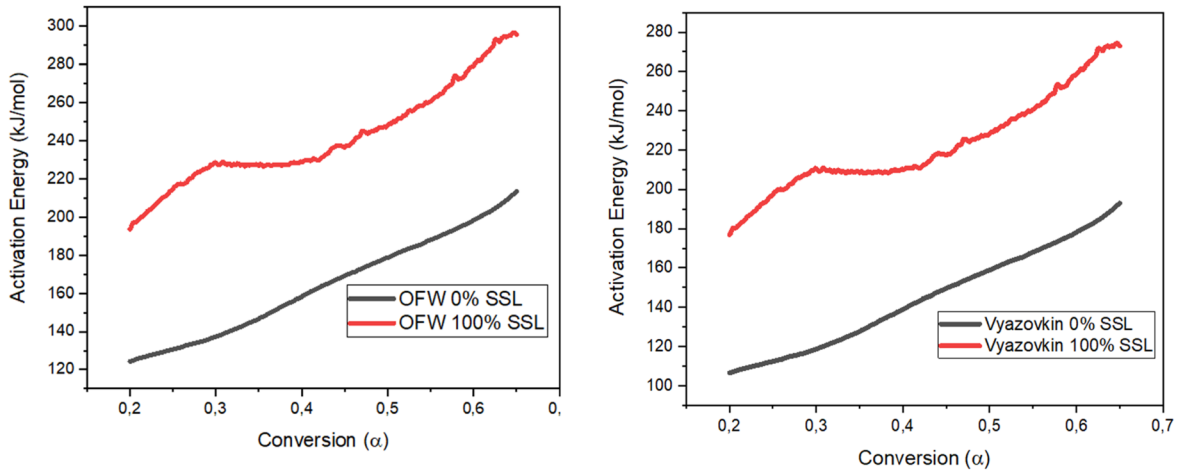

Fig. 10 OFW and Vyazovkin activation energies for sawdust and SSL.

To the best of the authors' knowledge, no previous studies have reported the use of isoconversional methods to determine the activation energies of SSL.

Table 7 summarizes the mean activation energies of sawdust, SSL, and their blends, calculated using two isoconversional methods over the conversion range $\alpha = 0.2$–0.8. SSL exhibited consistently higher activation energies than sawdust, which can be attributed to its higher lignin content, as discussed earlier. In contrast, sawdust–SSL blends showed lower activation energies compared to SSL alone, indicating improved thermal reactivity.

A notable reduction in activation energy was observed for blends containing 50–80% SSL. At 80% SSL, activation energy decreased by 18.92% and 20.23% for the OFW and Vyazovkin methods, respectively. This reduction is likely due to synergistic interactions between sawdust and SSL, particularly the influence of alkali and alkaline earth metals on lignocellulosic decomposition. Previous studies have highlighted the catalytic role of these metals in lowering activation energy during biomass pyrolysis.[24,69]

Kim *et al.*, (2019)[70] modelled the interaction between lignin and Mg and Na, reporting that magnesium increased the activation energy of lignin from 180 to 208 kJ mol^{-1}. Although magnesium exhibited a strong catalytic effect by elongating the C_β–O, dissociation bond and significantly reducing stabilizing energy,[70] it also enhanced the recalcitrance of lignin decomposition. The incorporation of sawdust, which contains higher proportions of cellulose and hemicellulose compared to SSL, may help mitigate this recalcitrance, thereby contributing to the overall reduction in activation energy observed in the blends.

3.3.3.1. Evolved gases. In addition to the well-known Diebold mechanism of cellulose decomposition,[71] Gu *et al.* (2013),[72] proposed a further mechanism decomposition of hemicellulose and lignin. These gases (CO_2, H_2O, CH_4, C_2H_6 and H_2) from SD and SSL which are rich lignocellulosic biomass that are proposed to be released during pyrolysis are shown in Fig. 11 and 12.

Fig. 11 shows the gases evolved (CO_2, H_2O and SO_2) from the pyrolysis of the samples, SD, SSL and SD-SSL. Carbon dioxide (CO_2) was the dominant gas, with significant release observed above 300 °C. SD exhibited the highest CO_2 concentration, followed closely by the SD–SSL blend, which slightly exceeded SSL.

Water vapor peaked around 100 °C for SD and dropped around 150 °C, SSL and SD-SSL blend continued to increase corresponding to the evaporation phase, which is also confirmed by the TG/DTG results. A secondary increase was noted above 300 °C, particularly in SD and SD–SSL. The elevated H_2O in SD–SSL compared to SSL alone implies that SD addition enhanced combustion, possibly by increasing the availability of reactive volatiles. Wang *et al.* (2021) propose the higher increase from the rapture of cellulose and hemicellulose above 350 °C.[73]

SD has no SO_2 detected, while SSL showed a markedly higher SO_2 concentration, consistent with its higher sulfur content. This confirms the presence of sulfur-bearing compounds in SSL, which decompose during pyrolysis.

The composition of hydrocarbons and hydrogen are shown in Fig. 12. The SD–SSL blend showed the highest H_2

Table 7 Mean activation energies of sawdust, SSL and their blends from three isoconversional method

Sample	Friedman method E_a (kJ mol^{-1})	OFW method E_a (kJ mol^{-1})	Vyazovkin method E_a (kJ mol^{-1})	A (s^{-1})	R^2
0% SSL	180.10	163.95	144.60	2.49×10^{14}	0.99
50% SSL	200.32	216.00	197.04	5.34×10^{7}	0.94
60% SSL	198.80	190.25	172.24	1.47×10^{6}	0.95
70% SSL	180.21	202.38	183.89	1.99×10^{7}	0.96
80% SSL	206.56	195.66	177.31	1.24×10^{7}	0.96
90% SSL	314.57	298.89	280.58	3.08×10^{7}	0.93
100% SSL	284.90	241.33	222.28	5.27×10^{8}	0.95

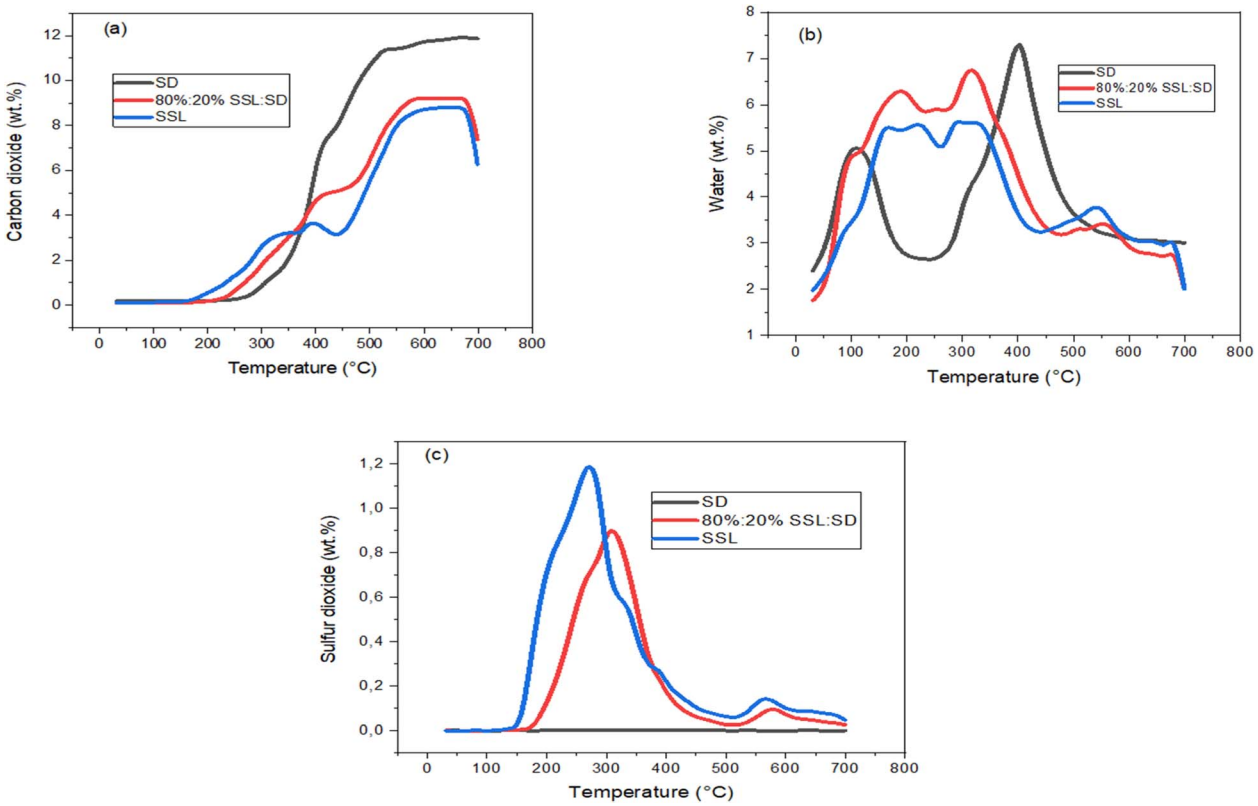

Fig. 11 Oxides evolved during pyrolysis of Sawdust, 80% MgSSL and 100% MgSSL (a) CO_2 (b) H_2O and (c) SO_2.

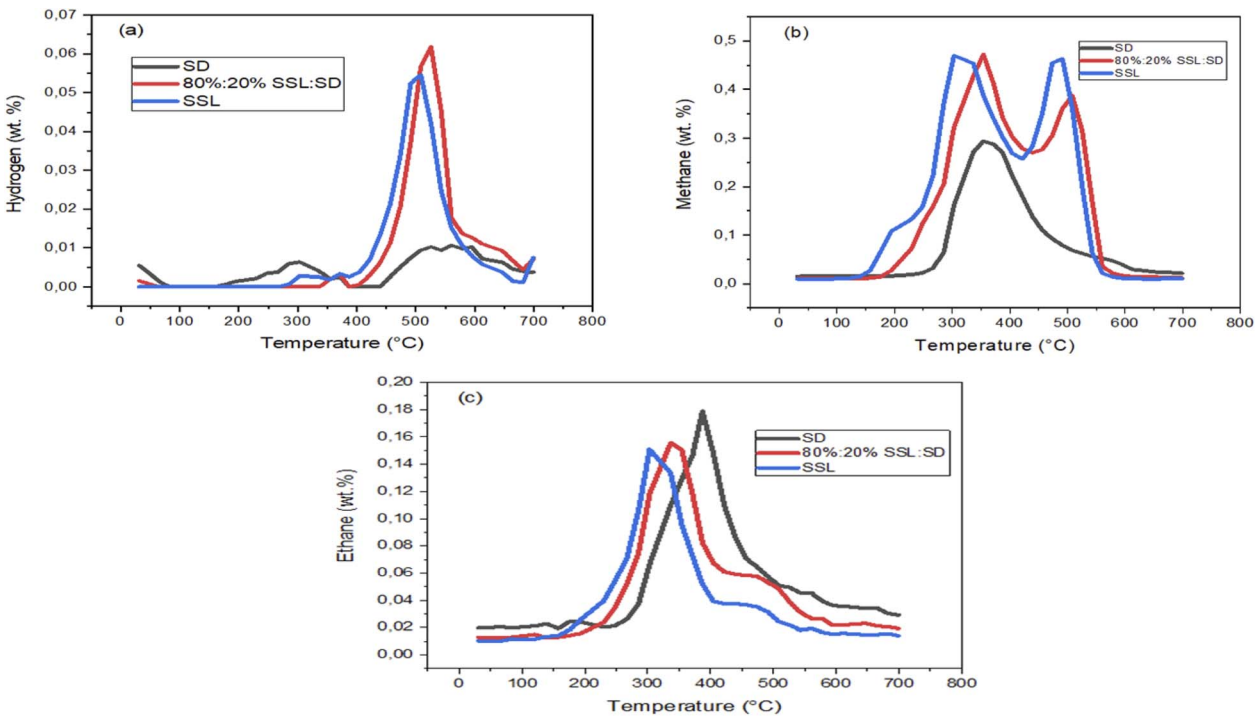

Fig. 12 Hydrocarbons and hydrogen gases evolved during pyrolysis of Sawdust, 80% MgSSL and 100% MgSS (a) H_2, (b) CH_4 and (c) C_2H_6.

concentration, exceeding 0.6 wt%, followed by SSL (~0.05 wt%). SD alone showed minimal H_2 evolution (<0.1 wt%). The proposed interaction during pyrolysis and secondary reaction (<400 °C) and main gas reactions are shown in eqn (11)–(16).[71]

$$\text{Tar} \rightarrow CH_4 + H_2 + C_mH_n + H_2 \quad (11)$$

$$C + H_2O \rightarrow CO + H_2 \quad (12)$$

$$CO + H_2O \rightarrow CO_2 + H_2 \quad (13)$$

$$C + CO_2 \rightarrow 2CO \quad (14)$$

$$C_mH_n + 2H_2O \rightarrow nCO_2 + \left[2n + \left(\frac{m}{2}\right)\right]H_2 \quad (15)$$

$$C_mH_n + H_2O \rightarrow nCO + \left[n + \left(\frac{m}{2}\right)\right]H_2 \quad (16)$$

This trend suggests that magnesium presence in SSL may enhance H_2 evolution, possibly through enhanced cracking or reforming reactions.

SSL exhibited a sharp CH_4 peak at 450 °C and 250 °C (~4.5 wt%), while SD–SSL showed similar peaks at 350 °C (wt% 4.5 wt%) and at 500 °C the peak fell slightly to (<4.0 wt%). The delayed peak in SSL may be due to slower decomposition of lignin or sulfur-containing compounds.

SD had the highest C_2H_6 concentration (~1.8 wt%), followed by SD–SSL (~1.6 wt%), and SSL slightly lower. This suggests that SD contributes more to light hydrocarbon formation, likely due to its cellulose-rich structure.

4. Conclusion

This study investigated the thermal decomposition of sawdust (SD) and spent sulfite liquor (SSL) using thermogravimetric analysis (TGA) to assess the kinetics, synergistic effects as well as gas evolved during co-pyrolysis. The catalytic influence of inherent alkali and alkaline earth metals in SSL remains an area of active research, and our findings provide new insights into their role during thermal conversion.

The results revealed that co-pyrolysis of SD and SSL exhibits a pronounced synergistic effect (ΔW), particularly at 70% and 80% SSL across different heating rates. This synergy lowered the decomposition temperature peaks of sawdust and contributed to improved thermal reactivity. Importantly, the introduction of sawdust reduced the activation energy (E_a) of the blends, with the most significant decrease–up to 20%, observed at 70% SSL. This reduction was confirmed using three isoconversional methods (Friedman, FWO, and Vyazovkin), highlighting the kinetic advantage of blending SD with SSL. The consistent char yield of SSL across all heating rates, despite sawdust addition, further emphasizes the stability of SSL during co-pyrolysis.

Evolved gas analysis revealed distinct selectivity patterns among the sample, demonstrating the potential for targeted gas production. The 80% SSL:20% SD blend exhibited favourable hydrogen evolution (>0.6 wt% near 550 °C), suggesting its suitability for hydrogen-rich gas generation which the magnesium presence in SSL could have catalysed. Conversely, sawdust favoured ethane formation (~1.8 wt% at 400 °C), while SSL showed strong methane selectivity (~4.5 wt% near 500 °C). These findings indicate that co-pyrolysis not only improves kinetic performance but also enables selective gas production, making it a promising strategy for sustainable thermochemical conversion and fuel generation.

From a practical perspective, understanding the pyrolysis behaviour of these blends is essential for optimizing reaction conditions, particularly in determining the ideal SD–SSL ratio and operating temperature. Further research should explore the catalytic role of magnesium in enhancing pyrolysis and investigate whether the 20% SD:80% SSL blend can catalyse other thermal treatments such as combustion, gasification, and torrefaction. Comparative studies on energy balance and life cycle analysis (LCA) between co-pyrolysis and conventional Tomlinson recovery boilers would provide valuable insights into industrial feasibility.

Integrating sawdust into SSL recovery offers both process and environmental benefits. This approach enhances biomass utilization, reduces reliance on fossil fuels, and has the potential to lower greenhouse gas emissions, contributing to environmental sustainability. Additionally, the pulp and paper industry could benefit from reduced energy costs and improved resource efficiency. Overall, co-pyrolysis of SD and SSL represents a promising technique for valorising waste streams and advancing renewable energy solutions.

Author contributions

Conceptualization: [Nampe Majoe, Isaac Beas and Bilal Patel]; writing – original draft preparation: [Nampe Majoe]; writing – review and editing: [Nampe Majoe, Bilal Patel, Joshua Gorimbo and Isaac Beas]; funding acquisition: [Nampe Majoe], resources: [Nampe Majoe]; supervision: [Bilal Patel, Joshua Gorimbo and Isaac Beas].

Conflicts of interest

The authors declare there was no conflict of interest.

Data availability

The data supporting this article have been included as part of the manuscript.

Acknowledgements

Internal funding: University of South Africa and Durban University of Technology.

References

1 M. V. Pinkas and R. I. Cheropkina, TENDENCIES OF MANUFACTURE OF PACKING MATERIALS FROM CARDBOARD, *Collection of theses and videos prepared for the materials of the International Scientific Internet Conference*

(Issue 74) 6–7 February 2023, 2023, p. 148, on the website, https://www.konferenciaonline.org.ua/us/article/id-954/.
2 P. K. Kunam, *et al.*, Bio-based materials for barrier coatings on paper packaging, *Biomass Convers. Biorefinery*, 2024, **14**(12), 12637–12652, DOI: 10.1007/s13399-022-03241-2.
3 S. Balkissoon, J. Andrew and B. Sithole, Dissolving wood pulp production: a review, *Biomass Convers. Biorefinery*, 2023, **13**(18), 16607–16642, DOI: 10.1007/s13399-022-02442-z.
4 J. Kennedy and C. Knill, Biomaterials utilised in medical textiles: an overview. *Medical Textiles and Biomaterials for Healthcare*, 2006, pp. 3–22, DOI: 10.1533/9781845694104.1.3.
5 T. Shaikh, S. Chaudhari and A. Varma, Viscose rayon: a legendary development in the manmade textile, *Int. J. Eng. Res. Ind. Appl.*, 2012, **2**(5), 675–680.
6 Y. Liu, *et al.*, A novel process for efficient utilization of bamboo fiber resource in dissolving pulp production by fiber fractionation: Laboratory study and mill trials, *Bioresour. Technol.*, 2024, **395**, 130400, DOI: 10.1016/j.biortech.2024.130400.
7 P. Bajpai and P. Bajpai, Production of dissolving-grade pulp. *Biotechnology for Pulp and Paper Processing*, 2018. pp. 291–311, DOI: 10.1007/978-981-10-7853-8_15.
8 S. D. Stefanidis, *et al.*, A study of lignocellulosic biomass pyrolysis via the pyrolysis of cellulose, hemicellulose and lignin, *J. Anal. Appl. Pyrolysis*, 2014, **105**, 143–150, DOI: 10.1016/j.jaap.2013.10.013.
9 C. Chen, *et al.*, Cellulose (dissolving pulp) manufacturing processes and properties: A mini-review, *Bioresources*, 2016, **11**(2), 5553–5564, DOI: 10.5555/20163175679.
10 C. Duan, *et al.*, Comparison of acid sulfite (AS)-and prehydrolysis kraft (PHK)-based dissolving pulps, *Cellulose*, 2015, **22**, 4017–4026, DOI: 10.1007/s10570-015-0781-1.
11 R. Bi, *et al.*, Enhancing Kraft based dissolving pulp production by integrating green liquor neutralization, *Carbohydr. Polym. Technol. Appl.*, 2021, **2**, 100034, DOI: 10.1016/j.carpta.2021.100034.
12 K. Rullifank, *et al.*, Pulp and paper industry: An overview on pulping technologies, factors, and challenges, in *IOP Conference Series: Materials Science and Engineering*, IOP Publishing, 2020, DOI: 10.1088/1757-899X/845/1/012005.
13 N. Lankila, Autonomous Recovery Boiler. 2023.
14 P. Bajpai, *Black Liquor Gasification*, Elsevier, 2014.
15 G. Wang, *et al.*, Biorefinery System for Producing Energy and Biofuels Based on Black Liquor Gasification Technology, in *Biotic Resources*, CRC Press, 2023, p. 149–174.
16 N. Majoe, *et al.*, Catalytic influence of alkali and alkali earth metals in black liquor on the gasification process: a review, *Biomass Convers. Biorefinery*, 2024, 1–19, DOI: 10.1007/s13399-024-06251-4.
17 N. Kundariya, *et al.*, A review on integrated approaches for municipal solid waste for environmental and economical relevance: Monitoring tools, technologies, and strategic innovations, *Bioresour. Technol.*, 2021, **342**, 125982, DOI: 10.1016/j.biortech.2021.125982.
18 A. Demirbas and G. Arin, An overview of biomass pyrolysis, *Energy Sources*, 2002, **24**(5), 471–482, DOI: 10.1080/00908310252889979.
19 Y. Lu, *et al.*, Investigation on the catalytic effect of AAEMs on the pyrolysis characteristics of Changji oil shale and its kinetics, *Fuel*, 2020, **267**, 117287, DOI: 10.1016/j.fuel.2020.117287.
20 K. Zeng, *et al.*, Towards directional pyrolysis of xylan: Understanding the roles of alkali/alkaline earth metals and pyrolysis temperature, *Energy*, 2022, **254**, 124245, DOI: 10.1016/j.energy.2022.124245.
21 N. Liu, *et al.*, Effects of alkali and alkaline earth metals in biomass on co-pyrolysis characteristics and product distribution of coal and biomass, *Fuel*, 2025, **389**, 134551, DOI: 10.1016/j.fuel.2025.134551.
22 C. Peng, *et al.*, Pyrolysis of black liquor for phenols and impact of its inherent alkali, *Fuel Process. Technol.*, 2014, **127**, 149–156, DOI: 10.1016/j.fuproc.2014.06.020.
23 X. Wang, *et al.*, Study on the effect mechanism of Ca and Mg with different anion on lignocellulosic biomass pyrolysis, *J. Anal. Appl. Pyrolysis*, 2024, **177**, 106335, DOI: 10.1016/j.jaap.2023.106335.
24 W. Wang, *et al.*, Review on the catalytic effects of alkali and alkaline earth metals (AAEMs) including sodium, potassium, calcium and magnesium on the pyrolysis of lignocellulosic biomass and on the co-pyrolysis of coal with biomass, *J. Anal. Appl. Pyrolysis*, 2022, **163**, 105479, DOI: 10.1016/j.jaap.2022.105479.
25 Q. Zhang and K. T. Chuang, Kinetics of wet oxidation of black liquor over a Pt–Pd–Ce/alumina catalyst, *Appl. Catal., B*, 1998, **17**(4), 321–332, DOI: 10.1016/S0926-3373(98)00016-2.
26 P. Šimon, *J. Therm. Anal. Calorim.*, 2004, **76**, 123–132, DOI: 10.1023/B:JTAN.0000027811.80036.6c.
27 K. Açıkalın, Determination of kinetic triplet, thermal degradation behaviour and thermodynamic properties for pyrolysis of a lignocellulosic biomass, *Bioresour. Technol.*, 2021, **337**, 125438, DOI: 10.1016/j.biortech.2021.125438.
28 P. K. Vimalathithan, C. Barile and C. T. Vijayakumar, Investigation of kinetic triplets for thermal degradation of thermally cured vinyl ester resin systems and lifetime predictions, *J. Therm. Anal. Calorim.*, 2018, **133**, 881–891, DOI: 10.1007/s10973-018-7154-6.
29 M. Li, *et al.*, Kinetic triplet determination and modified mechanism function construction for thermo-oxidative degradation of waste polyurethane foam using conventional methods and distributed activation energy model method, *Energy*, 2019, **175**, 1–13, DOI: 10.1016/j.energy.2019.03.032.
30 Y. Zhao, *et al.*, Kinetic study on pyrolysis of NSSC black liquor in a nitrogen atmosphere, *Chem. Eng. Commun.*, 2010, **197**(7), 1033–1047, DOI: 10.1080/00986440903359418.
31 X. Song, *et al.*, Kinetics of Reed Black Liquor (RBL) Pyrolysis from Thermogravimetric Data, *Bioresources*, 2015, **10**(1), 137–144.
32 L. N. Samuelsson, *et al.*, Pyrolysis of kraft pulp and black liquor precipitates derived from spruce: Thermal and kinetic analysis, *Fuel Process. Technol.*, 2016, **149**, 275–284, DOI: 10.1016/j.fuproc.2012.05.014.
33 S. P. Singh, Application of weibull mixture model to illustrate wheat straw black liquor pyrolysis kinetics, *SN*

Appl. Sci., 2020, **2**(12), 2022, DOI: 10.1007/s42452-020-03861-1.

34 M. Alam, *et al.*, Co-pyrolysis of bamboo sawdust and plastic: synergistic effects and kinetics, *Renewable Energy*, 2020, **149**, 1133–1145, DOI: 10.1016/j.renene.2019.10.103.

35 L. Florentino-Madiedo, *et al.*, Evaluation of synergy during co-pyrolysis of torrefied sawdust, coal and paraffin. A kinetic and thermodynamic study, *Fuel*, 2021, **292**, 120305, DOI: 10.1016/j.fuel.2021.120305.

36 E. Tarani and K. Chrissafis, Isoconversional methods: A powerful tool for kinetic analysis and the identification of experimental data quality, *Thermochim. Acta*, 2024, **733**, 179690, DOI: 10.1016/j.tca.2024.179690.

37 M. E. Brown, D. Dollimore, and A. K. Galwey, *Reactions in the Solid State*, Elsevier, 1980, vol. 22.

38 S. Vyazovkin, *Isoconversional Kinetics of Thermally Stimulated Processes*, Springer, 2015.

39 S. Vyazovkin and C. A. Wight, Model-free and model-fitting approaches to kinetic analysis of isothermal and nonisothermal data, *Thermochim. Acta*, 1999, **340**, 53–68, DOI: 10.1016/S0040-6031(99)00253-1.

40 J. Cai, *et al.*, Processing thermogravimetric analysis data for isoconversional kinetic analysis of lignocellulosic biomass pyrolysis: Case study of corn stalk, *Renew. Sustain. Energy Rev.*, 2018, **82**, 2705–2715, DOI: 10.1016/j.rser.2017.09.113.

41 H. L. Friedman, Kinetics of thermal degradation of char-forming plastics from thermogravimetry. Application to a phenolic plastic, *J. Polym. Sci., Part C, Polym. Symp.*, 1964, DOI: 10.1002/polc.5070060121.

42 Z. Zhang, *et al.*, Insight into kinetic and Thermodynamic Analysis methods for lignocellulosic biomass pyrolysis, *Renewable Energy*, 2023, **202**, 154–171, DOI: 10.1016/j.renene.2022.11.072.

43 Z. Zhang, X. Zheng and J. Cai, Modified Friedman isoconversional kinetic method for effective activation energies of waste tires rubber pyrolysis, *React. Kinet. Mech. Catal.*, 2024, 1–15, DOI: 10.1007/s11144-024-02629-7.

44 G. Berčič, The universality of Friedman's isoconversional analysis results in a model-less prediction of thermodegradation profiles, *Thermochim. Acta*, 2017, **650**, 1–7, DOI: 10.1016/j.tca.2017.01.011.

45 N. V. Muravyev, *et al.*, The power of model-fitting kinetic analysis applied to complex thermal decomposition of explosives: reconciling the kinetics of bicyclo-HMX thermolysis in solid state and solution, *J. Therm. Anal. Calorim.*, 2022, 1–12, DOI: 10.1007/s10973-021-10686-6.

46 N. V. Muravyev, A. N. Pivkina and N. Koga, Critical appraisal of kinetic calculation methods applied to overlapping multistep reactions, *Molecules*, 2019, **24**(12), 2298, DOI: 10.3390/molecules24122298.

47 J. Kristanto, *et al.*, Kinetic study on the slow pyrolysis of isolated cellulose and lignin from teak sawdust, *Thermochim. Acta*, 2022, **711**, 179202, DOI: 10.1016/j.tca.2022.179202.

48 T. Ozawa, A new method of analyzing thermogravimetric data, *Bull. Chem. Soc. Jpn.*, 1965, **38**(11), 1881–1886.

49 K. P. Kgatlane, *et al.*, Thermogravimetric-mass spectrometry study of pyrolysis of Botswana-Morupule coal: kinetic parameters determination using iso-conversional and model fitting methods, *React. Kinet. Mech. Catal.*, 2023, **136**(4), 2343–2358, DOI: 10.1007/s11144-023-02459-z.

50 J. H. Flynn and L. A. Wall, A quick, direct method for the determination of activation energy from thermogravimetric data, *J. Polym. Sci. B Polym. Lett.*, 1966, **4**(5), 323–328.

51 S. Vyazovkin, Modification of the integral isoconversional method to account for variation in the activation energy, *J. Comput. Chem.*, 2001, **22**(2), 178–183, DOI: 10.1002/1096-987X(20010130)22:2<178::AID-JCC5>3.0.CO;2-%23.

52 S. Vyazovkin, Evaluation of activation energy of thermally stimulated solid-state reactions under arbitrary variation of temperature, *J. Comput. Chem.*, 1997, **18**(3), 393–402, DOI: 10.1002/(SICI)1096-987X(199702)18:3<393::AID-JCC9>3.0.CO.

53 D. Drozin, *et al.*, Kinetic calculation: Software tool for determining the kinetic parameters of the thermal decomposition process using the Vyazovkin Method, *SoftwareX*, 2020, **11**, 100359, DOI: 10.1016/j.softx.2019.100359.

54 N. Duangkaew, *et al.*, Utilization of black-liquor by hydrothermal liquefaction, *Mater. Today: Proc.*, 2023, **75**, 99–105, DOI: 10.1016/j.matpr.2022.11.227.

55 A. K. Varma, *et al.*, Pyrolysis of wood sawdust: Effects of process parameters on products yield and characterization of products, *Waste Manage.*, 2019, **89**, 224–235, DOI: 10.1016/j.wasman.2019.04.016.

56 H. P. le Roux, *et al.*, The use of spent liquors from paper and pulp industry as binders for the pelletization of chromite fines, *Miner. Eng.*, 2024, **216**, 108846, DOI: 10.1016/j.mineng.2024.108846.

57 A. Trada, *et al.*, An alternative fuel production from sawdust through batch-type pyrolysis reactor: Fuel properties and thermodynamic analysis, *Process Saf. Environ. Prot.*, 2022, **167**, 332–342, DOI: 10.1016/j.psep.2022.09.023.

58 E. Ceylan, *et al.*, Effect of solvent type and pH degree on the chemical composition of kraft black liquor via ARAS method, *Wood Sci. Technol.*, 2023, **57**(3), 741–757, DOI: 10.1007/s00226-023-01467-5.

59 H. Yang, *et al.*, Characteristics of hemicellulose, cellulose and lignin pyrolysis, *Fuel*, 2007, **86**(12–13), 1781–1788, DOI: 10.1016/j.fuel.2006.12.013.

60 M. Guida, *et al.*, Thermal degradation behaviors of sawdust wood waste: pyrolysis kinetic and mechanism, *J. Mater. Environ. Sci.*, 2019, **10**(8), 742–755.

61 R. K. Mishra and K. Mohanty, Pyrolysis kinetics and thermal behavior of waste sawdust biomass using thermogravimetric analysis, *Bioresour. Technol.*, 2018, **251**, 63–74.

62 Y. Song, A. Tahmasebi and J. Yu, Co-pyrolysis of pine sawdust and lignite in a thermogravimetric analyzer and a fixed-bed reactor, *Bioresour. Technol.*, 2014, **174**, 204–211, DOI: 10.1016/j.biortech.2014.10.027.

63 M. Poletto, Assessment of the thermal behavior of lignins from softwood and hardwood species, *Maderas Cienc.*

Tecnol., 2017, **19**(1), 63–74, DOI: 10.4067/S0718-221X2017005000006.

64 R. Alén, S. Rytkönen and P. McKeough, *J. Anal. Appl. Pyrolysis*, 1995, **31**, 1–13, DOI: 10.1016/0165-2370(94)00811-E.

65 B. Khiari and M. Jeguirim, Pyrolysis of grape marc from Tunisian wine industry: Feedstock characterization, thermal degradation and kinetic analysis, *Energies*, 2018, **11**(4), 730.

66 A. Nyombi, M. Williams and R. Wessling, Determination of kinetic parameters and thermodynamic properties for ash (Fraxinus) wood sawdust slow pyrolysis by thermogravimetric analysis, *Energy Sources, Part A Recovery, Util. Environ. Eff.*, 2018, **40**(22), 2660–2670.

67 J. Wang, *et al.*, Understanding pyrolysis mechanisms of pinewood sawdust and sugarcane bagasse from kinetics and thermodynamics, *Ind. Crops Prod.*, 2022, **177**, 114378, DOI: 10.1016/j.indcrop.2021.114378.

68 R. Yang, X. Lu and X. Gu, Pyrolysis kinetics of a lignin-modified cellulose composite film, *ACS Omega*, 2021, **6**(51), 35584–35592, DOI: 10.1021/acsomega.1c05289.

69 A. Saddawi, J. Jones and A. Williams, Influence of alkali metals on the kinetics of the thermal decomposition of biomass, *Fuel Process. Technol.*, 2012, **104**, 189–197, DOI: 10.1016/j.fuproc.2012.05.014.

70 K. H. Kim, *et al.*, Kinetic understanding of the effect of Na and Mg on pyrolytic behavior of lignin using a distributed activation energy model and density functional theory modeling, *Green Chem.*, 2019, **21**(5), 1099–1107, DOI: 10.1039/c8gc02948b.

71 J. P. Diebold, A unified, global model for the pyrolysis of cellulose, *Biomass Bioenergy*, 1994, **7**(1–6), 75–85, DOI: 10.1016/0961-9534(94)00039-V.

72 X. Gu, *et al.*, Pyrolysis of poplar wood sawdust by TG-FTIR and Py–GC/MS, *J. Anal. Appl. Pyrolysis*, 2013, **102**, 16–23, DOI: 10.1016/j.jaap.2013.04.009.

73 B. Wang, Y. Li and J. Zhou, Thermogravimetric and kinetic analysis of high-temperature thermal conversion of pine wood sawdust under CO2/Ar, *Energies*, 2021, **14**, 5328.